SCIENTIFIC REPORTS

natureresearch

OPEN

Concentration-Diversified Magnetic and Electronic Properties of Halogen-Adsorbed Silicene

Duy Khanh Nguyen[1,2], Ngoc Thanh Thuy Tran[3], Yu-Huang Chiu[4] & Ming-Fa Lin[5]

Diverse magnetic and electronic properties of halogen-adsorbed silicene are investigated by the first-principle theoretical framework, including the adatom-diversified geometric structures, atom-dominated energy bands, spatial spin density distributions, spatial charge density distributions and its variations, and orbital-projected density of states. Also, such physical quantities are sufficient to identify similar and different features in the double-side and single-side adsorptions. The former belongs to the concentration-depended finite gap semiconductors or p-type metals, while the latter display the valence energy bands with/without spin-splitting intersecting with the Fermi level. Both adsorption types show the halogen-related weakly dispersed bands at deep energies, the adatom-modified middle-energy σ bands, and the recovery of low-energy π bands during the decrease of the halogen concentrations. Such feature-rich band structures can be verified by the angle-resolved photoemission spectroscopy experiment.

A new era of material sciences has arisen since the successful fabrication of two-dimensional (2D) graphene[1,2]. Such a 2D planar carbon structure with a hexagonal lattice exhibits many exceptional properties, including massless Dirac fermions, strength of the lattice structure, high thermal conductivity, and half-integer Hall conductance[3–5]. However, the lack of an energy gap makes graphene incompatible for practical applications. Therefore, how to induce a band gap is an important issue to make use of graphene as a real material and provides a strong motivation for studies on graphene composites/graphene-like 2D materials[6–8]. The graphene composite materials with a sizable band gap consisting of grapheneoxide (GO)[9,10], graphane (HO)[11–13], fluorographene (CF)[14,15], and chlorographene (CCl)[16,17] have investigated in previous studies. Also, the graphene-like 2D monolayers of BN are explored in a stable structure[18,19]. Such a BN system is a wide gap insulator with an energy gap of 4.6 eV even though BN has the same 2D planar honeycomb structure as graphene[20]. Therefore, the tiny lattice mismatch in the graphene/BN contact renders it possible to construct nanoscale electronic devices[21]. Furthermore, graphene-like 2D materials comprised of group IV elements, which possess a buckled honeycomb structure with a mix of sp²/sp³ hybridization formed by four outermost-orbital valence electrons, contain a variety of potential properties and have attracted tremendous attention in the fields of physics, chemistry, and materials science, especially the low buckled 2D silicon structures[22–26].

Though the premature allotrope forms of silicon, nanotubes[27] and fullerene[28], were early identified, a 2D silicon structure does not seem to exist in nature owing to the absence of a solid phase of silicon. As a result, monolayer silicene is impossible to synthesize by exfoliation methods as initially utilized for graphene. Other possible methods are advanced for the growth of silicene. The most feasible method is to deposit silicon atoms on metal surfaces (silver or iridium) that do not interact strongly with Si atoms or create compounds[29–32], providing the direct evidence for the presence of 2D silicon sheets which were theoretically predicted in 1994[33]. Formation energy and phonon dispersion calculations have determined that silicene is energetically favorable in a low buckled honeycomb structure[34]. The electronic structure of pristine silicene presents a negligible energy gap, in which the energy bands linearly cross at the Fermi level. This feature might attribute a massless Dirac

[1]Laboratory of Applied Physics, Advanced Institute of Materials Science, Ton Duc Thang University, Ho Chi Minh City, Vietnam. [2]Faculty of Applied Sciences, Ton Duc Thang University, Ho Chi Minh City, Vietnam. [3]Hierarchical Green-Energy Materials (Hi-GEM) Research Center, National Cheng Kung University, Tainan, 701, Taiwan. [4]Department of Applied Physics, National Pingtung University, Pingtung, Taiwan. [5]Department of Physics/QTC/Hi-GEM, National Cheng Kung University, Tainan, Taiwan. Correspondence and requests for materials should be addressed to D.K.N. (email: nguyenduykhanh@tdtu.edu.vn) or Y.-H.C. (email: yhchiu@mail.nptu.edu.tw) or M.-F.L. (email: mflin@mail.ncku.edu.tw)

fermion characteristic to charge carriers, which has been verified by angle-resolved photoemission spectroscopy and scanning tunneling spectroscopy measurements[35,36]. The possible high carrier mobility make silicene an ideal material, especially for the applications in field effect transistors[37]. Other fundamental properties of silicene have been revealed, such as a large energy gap opened by the spin-orbit coupling at Dirac point[38], a quantum spin Hall effect observed in a low-temperature regime[39], transition from a topological insulating phase to a band insulator generated by an electric field and electrically tunable energy gap[40,41], and the emergence of a valley-polarized metal and anomalous quantum Hall effect[42]. Such potential properties identify silicene as a promising candidate to replace graphene not only due to the graphene-like features, but also its compatibility with silicon-based electronic devices.

Most intriguingly, the essential properties of silicene are extremely sensitive to chemical modifications. Among the chemical functionalizations, the atom dopings are one of the effective methods to dramatically change the fundamental properties. Hydrogen-adsorbed silicene exhibits semiconducting or metallic behavior that depend on the adatom concentrations[43]. The metalization of silicene, narrow gap semiconductor, and the semi-metallic or semiconducting behavior are revealed in alkali (Li, Na, K)-, alkali-earth (Be, Mg, Ca)-, and 3d transition metal atom (Ti, V, Cr, Mn, Fe, Co, Mo, and W)-adsorbed silicenes, respectively[44]. Besides, the chemical functionalization of silicene with boron (B), nitrogen (N), aluminum (Al), and phosphorus (P) adatoms have been explored in detail. Such systems present a metallic behavior with strongly bonded B, N, Al, and P adatoms, in which there exists the electron transfer from Si atoms to B, N, and P adatoms (p-type doping), and the opposite charge transfer (n-type doping) with weaker bonding for Al adatoms[45]. Furthermore, the electronic properties and optimal structure models of halogenated silicene have been explored by first-principles studies and low-temperature scanning tunneling microscopy measurements, respectively[46–48]. However, those studies mainly focused on a specific halogen concentration. As a result, the various halogenation effects on 2D silicene deserve a further look because of its promising applications, especially for electrode materials in lithium-ion battery.

In this work, the geometric, magnetic, and electronic properties of halogen-adsorbed silicene are fully investigated by the first-principle study. The double-side [Fig. 1(a)] and single-side [Fig. 1(b)] adsorptions are considered in calculations to evidence that these adsorption types can present the diverse magnetic and electronic properties, in which they are determined by the adatom-diversified geometric structures, atom-dominated energy bands, the spatial spin density distributions, the spatial charge density distributions and its difference, and the orbital-projected density of states (DOSs). Via such physical quantities, the similar and different characteristics in double-side and single-side adsorption cases are thoroughly identified, including the halogen-related weakly dispersed bands at deep energies, the adatom-modified middle-energy σ bands, the recovery of low-energy π bands during the decrease of the halogen concentrations; however, the breaking of the mirror symmetry in the single-side adsorptions leads to the critical discrepancy, i.e., there appear the valence energy bands with/without spin-splitting intersecting with the Fermi level as a result of p-type metallic behavior. The predicted results in the geometric structures, band structures, and DOSs can be verified by the scanning tunneling microscopy (STM), angle-resolved photoemission spectroscopy (ARPES), and scanning tunneling spectroscopy (STS) experiments, respectively.

Result and Discussion

Geometric structure. The ab initio calculations are performed in order to explore the geometric, magnetic, and electronic properties of halogen-adsorbed silicene under the various concentrations. Two typical adsorption types of fully halogenated silicene are chosen for this systematic study. The double-side adsorption, in which both sides of the silicene plane are thoroughly covered by halogen adatoms, as shown in Fig. 1(a). The halogen adatoms are uniformly distributed so that each adatom is separated by its six nearest adatoms with the same distance [Fig. 1(c)], and the back-side adatoms (green balls) are set in the middle of three front-side adatoms (red balls). For the single-side adsorption, the adatoms only cover a single side of the silicene plane [Fig. 1(b)], i.e., all the back-side adatoms are removed so that the concentration is reduced to half of the double-side adsorption. The typical concentrations vary from 100%, 12,5%, and 5,6%, where the ratios between halogen adatoms and Si atoms correspond to 2:2, 1:8 and 1:18, respectively [Fig. 1(c)]; more cases are shown in Tables 1 and 2. The binding energy is calculated by $E_b = (E_T - E_P - \text{n} E_A)/\text{n}$, in which the E_T, E_P, and E_A are, respectively, the energies of the fully halogen adsorbed silicene, pristine silicene, and isolated halogen adatoms; n represents the number of halogen adatoms. The lower binding energy corresponds to a higher stability. The most optimal geometric symmetry is used in the calculations. Via the detailed examinations, the most optimal adsorption position is situated at the top site (on the top of the upper silicon atom), as compared with the hollow site (above the center of the hexagonal silicon ring), valley site (on the top of the lower silicon atom), and bridge site (on the top of the Si-Si bond), irrespective of any doping case[45]. Among the halogen adatoms, the magnitude of binding energy declines with the increase of the atomic number [Tables 1 and 2], i.e., the F-adsorbed systems achieve the lowest binding energy ~ −5.3 eV–−4.7 eV. Furthermore, the halogen-absorbed silicene [Tables 1 and 2] possesses a higher geometric stability than halogen-adsorbed graphene[49] because of its highly reactive buckled surface. The shortest halogen-Si bond length is revealed in the F-adsorbed system ~1.63 Å–1.64 Å, due to its smallest atomic number among halogen atoms. The stable halogen-Si bondings are formed by the transfer of electrons from Si atoms to halogen adatoms (discussed in the charge distribution section), and they are almost insensitive to the adatom concentration. The charge transfer renders the nearest Si-Si bonds weakened, i.e., the nearest Si-Si bond lengths are lengthened (2.31 Å–2.33 Å) as compared with the pristine Si-Si bond length (2.25 Å). The Si-Si bonds nearest to the halogen adatom are termed as the nearest Si-Si bonds. Besides, the halogen-Si-Si bond angles increase and buckling structures become obvious when the adatom concentration declines [Tables 1 and 2]. It is notable that in a pristine silicene, the planar Si-Si bondings are formed by Si-(3 s, $3p_x$, $3p_y$) orbitals, while the π-π overlap of the parallel $3p_z$ orbitals of nearest Si atoms reduces in strength, and thus Si atoms have a mix of sp^2/sp^3 hybridization; therefore, the adatom adsorption on silicene could be easier to tune than purely sp^2 hybridized graphene. When the halogen
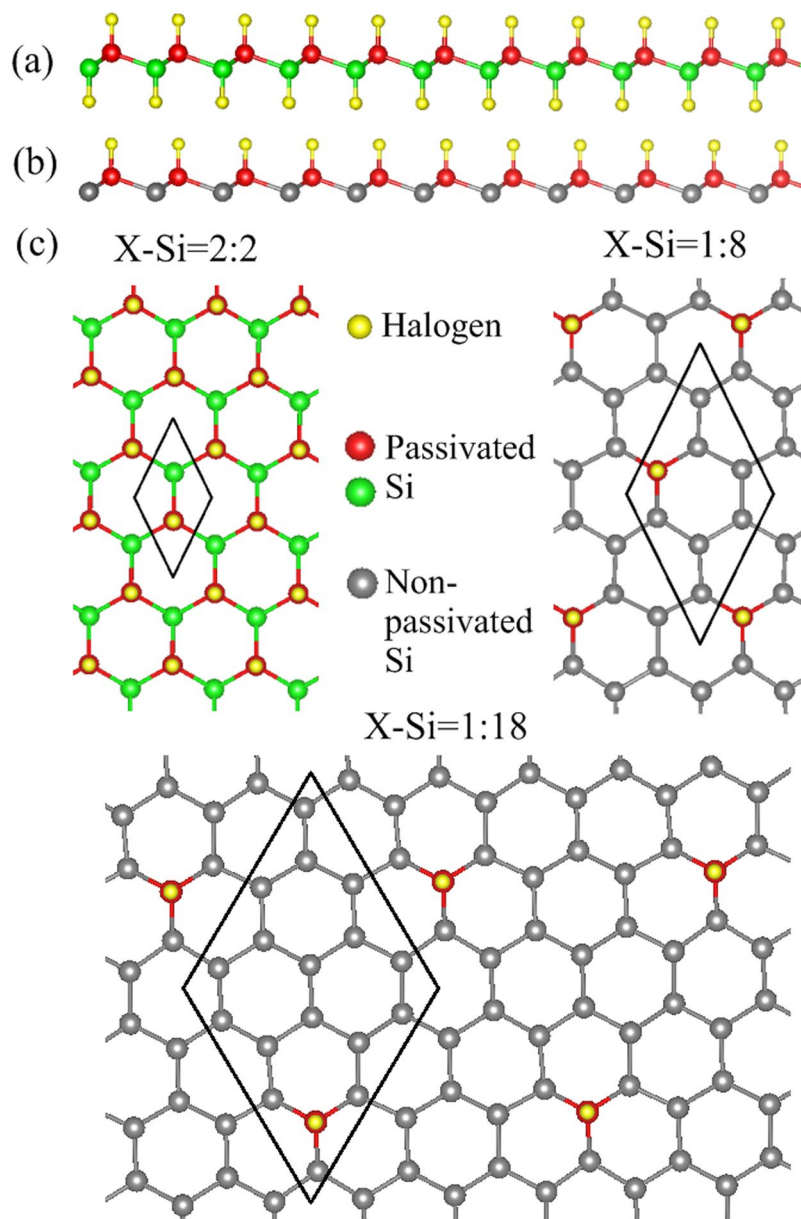
Figure 1. Side-view geometric structures of halogenated silicene for (**a**) double-side adsorption and (**b**) single-side adsorption. (**c**) top-view geometric structures of various halogen (X) concentrations, including X-Si = 2:2, X-Si = 1:8, and X-Si = 1:18.

adatoms are bonded with Si atoms, the Si atoms are changed from a mix of sp^2/sp^3 hybridization to sp^3 hybridization. The chemical bonding scheme is determined by the hybridization between the Si-$3p_z$ orbitals and halogen-(p_x, p_y, and p_z) orbitals, and the weak sp^3 hybridization of four orbitals ($3s$, $3p_x$, $3p_y$, and $3p_z$). The double-side and single-side adsorptions present similar geometric distortions; however, they might lead to different electronic and magnetic properties, mainly owing to the broken mirror symmetry [Fig. 1(b)].

For experimental verification, STM is a powerful instrument for imaging surfaces at the atomic level. This tool can directly detect the surface structures in real-space under the atomic resolution, including the atomic lattice, the very short bond lengths, the planar or buckled structures, the achiral or chiral edges, the surface adsorptions, and the atom substitutions. Up to date, high-resolution STM observations have successfully verified the atomic structures of graphenes[50], few-layer graphenes[51], hydrogenation of graphenes[52], fluorinated graphenes on copper[53], 1D graphene nanoribbons[54], silicene layers grown on Ag(111)[30], silicene nanoribbons on Ag(110)[55], hydrogenation of silicene films grown on Ag(111)[56], chlorination of monolayer silicenes[48], and multilayer silicenes[57]. Apparently, the predicted results in the buckled silicene after halogen adsorptions, including the top-site positions of halogen adatoms, halogen-Si & Si-Si bond lengths, buckling structures, and bond angles could be verified by high-resolution STM measurements, being very useful in confirming the multi-orbital hybridizations in the chemical bonds.

Ratio of adatom and Si	E_b (eV)	Magnetic moment (μ_B)/magnetism	E_g^d (eV)/M/SM	adatom-Si (Å)	Near-est Si-Si (Å)	adatom –Si –Si angle (°)	Δ (Å)
Pristine	X	0/NM	$E_g^d = 0.001$	X	2.255	X	0.490
F:Si = 2:2	−5.29490	0/NM	$E_g^d = 0.47$	1.631	2.322	109.12	0.760
F:Si = 8:8	−5.29490	0/NM	$E_g^d = 0.47$	1.631	2.322	109.12	0.760
F:Si = 6:8	−5.38383	0/NM	$E_g^i = 0.81$	1.630	2.335	109.63	0.762
F:Si = 4:8	−5.32565	0/NM	$E_g^i = 0.78$	1.630	2.332	109.67	0.763
F:Si = 2:8	−5.31450	0/NM	$E_g^i = 0.75$	1.639	2.319	110.42	0.771
F:Si = 2:18	−5.39129	0/NM	M	1.637	2.318	111.92	0.887
F:Si = 2:32	−5.45832	0/NM	M	1.641	2.318	113.96	0.910
Cl:Si = 2:2	−3.22631	0/NM	$E_g^d = 1.16$	2.071	2.328	109.52	0.778
Cl:Si = 8:8	−3.22685	0/NM	$E_g^d = 1.16$	2.071	2.328	109.52	0.778
Cl:Si = 4:8	−3.29581	0/NM	$E_g^i = 0.93$	2.087	2.330	109.69	0.782
Cl:Si = 2:8	−3.26759	0/NM	$E_g^i = 0.83$	2.096	2.321	109.83	0.785
Cl:Si = 2:18	−3.38563	0/NM	M	2.096	2.322	111.74	0.881
Cl:Si = 2:32	−3.39675	0/NM	M	2.097	2.321	111.91	0.898
Br:Si = 2:2	−2.41261	0/NM	$E_g^d = 1.09$	2.240	2.326	109.42	0.772
Br:Si = 8:8	−2.41256	0/NM	$E_g^d = 1.09$	2.240	2.326	109.42	0.772
Br:Si = 4:8	−2.75106	0/NM	$E_g^i = 0.96$	2.261	2.325	109.76	0.780
Br:Si = 2:8	−2.67977	0/NM	$E_g^i = 0.94$	2.274	2.320	109.98	0.791
Br:Si = 2:18	−2.79401	0/NM	M	2.274	2.320	111.54	0.864
Br:Si = 2:32	−2.83164	0/NM	M	2.276	2.320	111.72	0.902
I:Si = 2:2	−1.29362	0/NM	$E_g^d = 0.51$	2.459	2.326	109.41	0.772
I:Si = 8:8	−1.29426	0/NM	$E_g^d = 0.51$	2.459	2.326	109.41	0.772
I:Si = 4:8	−2.00385	0/NM	$E_g^i = 0.95$	2.485	2.313	110.63	0.785
I:Si = 2:8	−1.97356	0/NM	$E_g^i = 0.93$	2.507	2.320	110.95	0.789
I:Si = 2:18	−2.19425	0/NM	M	2.506	2.319	111.67	0.854
I:Si = 2:32	−2.20716	0/NM	M	2.508	2.320	111.92	0.893
At:Si = 2:2	−0.71032	0/NM	SM	2.584	2.326	109.43	0.772

Table 1. Binding energy (E_b) eV; magnetic moment/magnetism; energy gap ($E_g^{d(i)}$)/metal (M)/semi-metal (SM); halogen (adatom)-Si bond length (Å), Si-Si bond length (Å), adatom-Si-Si bond angle (°), and buckling (Δ) (Å) for the double-side adsorption under the various concentrations. NM and FM correspond to non-magnetism and ferro-magnetism, respectively.

Feature-rich band structure.   The 2D energy dispersions reveal a dramatic change under the competition between the halogen-Si bonding and the weak sp³ hybridization. The Brillouin zone scheme for various unit cells is presented in Fig. 2, in which all the band structures are plotted along Γ-K-M-Γ paths. A pristine silicene [Fig. 3(a)] exhibits a Dirac cone structure at the K point (corner of the blue hexagon in Fig. 2) owing to the extended π bondings of Si-3p$_z$ orbitals, and a negligible energy gap of 1 meV. The low-lying linear energy bands turn into parabolic dispersions with a saddle point at the M point, as shown in Fig. 3(a). These energy bands are mainly dominated by 3p$_z$ orbitals of the two nearest Si atoms, regarding as π bands. Moreover, the weak sp³ hybridization illustrates an obvious separation of the π bands and σ bands within ±2 eV. The occupied and unoccupied σ parabolic bands are respectively initiated at −1 eV and 1.2 eV, indicated by the black and red rectangles in Fig. 3(a). The highest occupied bands display a double degeneration at the Γ point, while the lowest unoccupied bands are non-degenerate at the M point. The former bands are mainly contributed by the (3p$_x$ and 3p$_y$) orbitals, and they are hybridized with the 3p$_z$ orbitals at lower energy of −2.5 eV. The third occupied σ band initiates at −1 eV, dominating by the 3 s orbitals, and gradually becomes parabolically dispersed. This band becomes partially flat at −3.2 eV near the Γ point, in which there exist an orbital hybridization between the 3 s orbitals and 3p$_z$ orbitals (discussed in DOSs section). These fundamental features are dramatically modified after halogen adsorptions.

The double-side adsorption cases exhibit semiconducting or metallic behaviors, depending on distinct concentrations. The fully fluorinated, chlorinated, brominated, and iodinated silicene present a direct energy gap of 0.47 eV, 1.16 eV, 1.09 eV, and 0.51 eV, as shown in Fig. 3(b,e–g), respectively. These gaps are determined by the highest occupied states (HOS) and lowest unoccupied states (LUS) at the Γ point, and their magnitudes do not have a linear relationship with their atomic numbers. Otherwise, fully astatinated silicene displays a semi-metallic behavior with an overlap of valence and conduction bands at the Fermi level near the Γ point owing to the very weak At-Si bonds [Fig. 3(h)]. The hybridization of Si-3p$_z$ orbitals and halogen-p$_z$ orbitals puts the π bands away from the Fermi level. Thus, the band gaps are determined by the σ bands. The middle-energy σ band of Si-(3p$_x$ and 3p$_y$) orbitals at −1 eV [Fig. 3(a)] is situated ∼ −0.2 eV [Fig. 3(b)] or ∼ −0.5 eV [Fig. 3(e,f)], meaning that such bands have a blue shift of ∼0.8 eV or ∼0.5 eV. This clearly indicates the Si-Si σ bondings display a small change after halogen adsorptions, observed by the lengthened nearest Si-Si bond lengths (discussed in the geometric structure

Ratio of adatom and Si	E_b (eV)	Magnetic moment (μ_B)/magnetism	$E_g^{d(i)}$ (eV)/M/SM	adatom –Si (Å)	Near-est Si-Si (Å)	adatom –Si -Si angle (°)	Δ (Å)
F:Si = 1:2	−4.76899	0/NM	M	1.633	2.321	109.04	0.763
F:Si = 4:8	−4.76846	0/NM	M	1.633	2.321	109.04	0.763
F:Si = 1:8	−5.12832	0.45/FM	M	1.636	2.315	114.24	0.949
F:Si = 1:18	−5.23563	0/NM	M	1.636	2.313	116.96	1.048
F:Si = 1:32	−5.31026	0/NM	M	1.637	2.313	117.40	1.064
Cl:Si = 1:2	−2.58719	0.72/FM	M	2.091	2.328	109.56	0.779
Cl:Si = 4:8	−2.58354	0.72/FM	M	2.091	2.328	109.56	0.779
Cl:Si = 1:8	−3.18866	0.64/FM	M	2.096	2.320	113.96	0.942
Cl:Si = 1:18	−3.28117	0/NM	M	2.099	2.320	117.12	1.057
Cl:Si = 1:32	−3.35039	0/NM	M	2.099	2.321	117.70	1.079
Br:Si = 1:2	−1.78324	0.89/FM	M	2.269	2.326	109.43	0.773
Br:Si = 4:8	−1.78228	0.89/FM	M	2.269	2.326	109.43	0.773
Br:Si = 1:8	−2.55506	0.67/FM	M	2.277	2.320	113.69	0.932
Br:Si = 1:18	−2.62592	0/NM	M	2.280	2.320	116.68	1.042
Br:Si = 1:32	−2.67667	0/NM	M	2.280	2.321	117.63	1.077
I:Si = 1:2	−0.83202	0.79/FM	M	2.566	2.336	110.08	0.802
I:Si = 4:8	−0.83172	0.79/FM	M	2.566	2.336	110.08	0.802
I:Si = 1:8	−1.96195	0.73/FM	M	2.512	2.319	113.22	0.913
I:Si = 1:18	−2.07592	0/NM	M	2.517	2.320	116.45	1.033
I:Si = 1:32	−2.08183	0/NM	M	2.517	2.322	117.42	1.070
At:Si = 1:2	−0.40616	0.82/FM	M	2.830	2.319	108.87	0.751

Table 2. Representation similar to that in Table 1, but shown for single-side adsorptions.
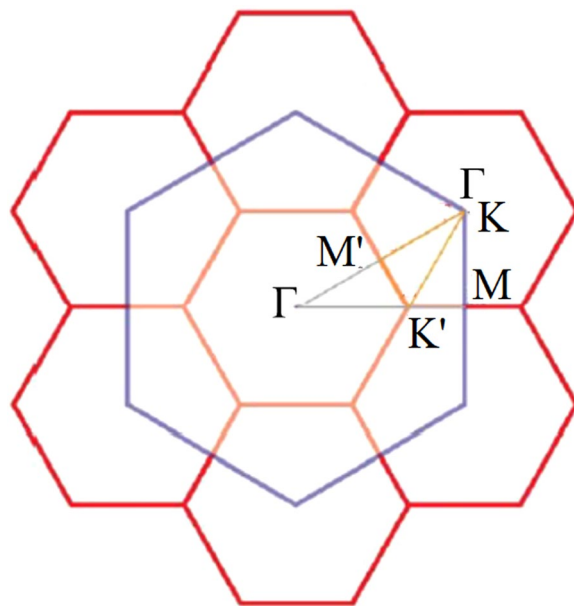

Figure 2. Brillouin zone scheme for different unit cells.

section) and the weakened nearest Si-Si bond strength (discussed in the spatial charge distribution section). Among halogen adatoms, F adatom-related weakly dispersed bands dominate at the deepest energies due to its shortest F-Si bond length [blue circles in Fig. 3(b)]. This band dispersion becomes more obvious and gradually dominates at higher energies with an increase of its atomic numbers, mainly owing to the higher halogen-Si bond lengths [blue circles Fig. 3(e–h)].

As the adatom concentration declines, the halogen-Si bonds reduce in number, and rather compete with the effect of the weak sp³ hybridization to determine the energy bands. Quite different from the 100% system, the 25% system presents an indirect energy gap of 0.75 eV, which is determined by HOS and LUS at the Γ and M points [Fig. 3(c) and Table 1]. The critical concentration is revealed at 11% [Fig. 3(d)], exhibiting the p-type metallic behavior, in which there exist valence energy bands intersecting with the Fermi level, so that the unoccupied
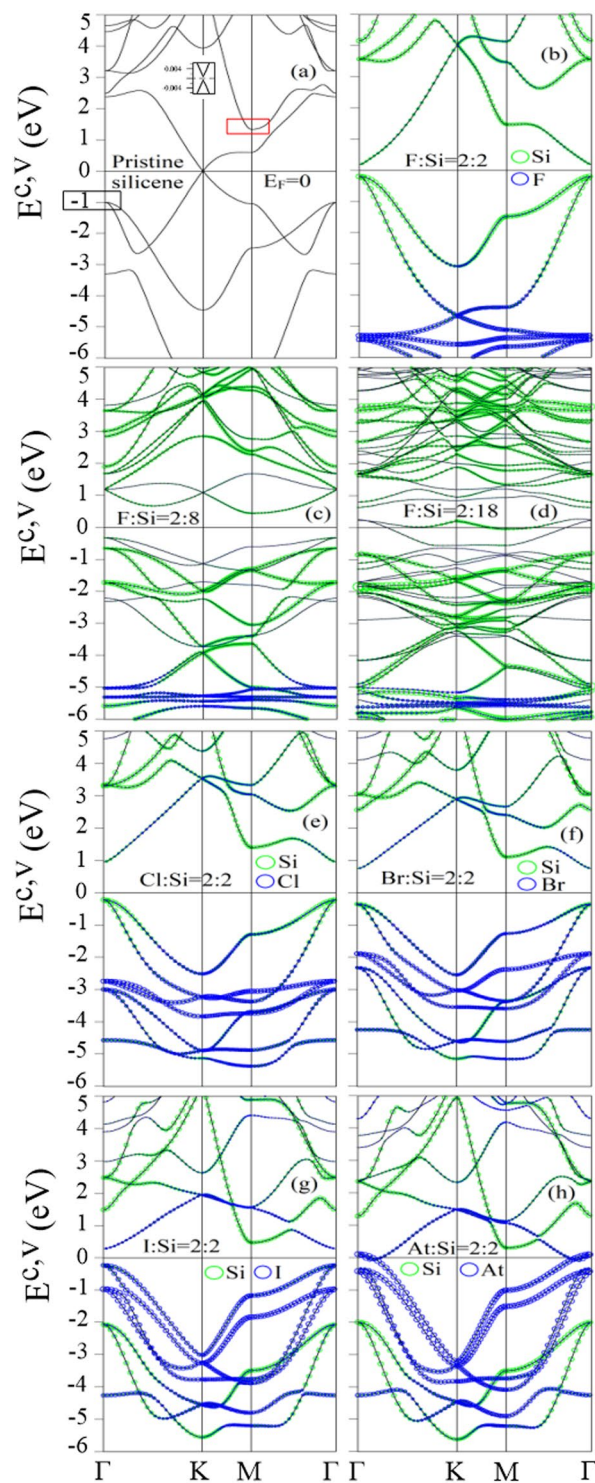
Figure 3. Electronic band structures of (**a**) pristine silicene and halogenated silicene under double-side adsorptions for (**b**) F:Si = 2:2, (**c**) F:Si = 2:8, (**d**) F:Si = 2:18, (**e**) Cl:Si = 2:2, (**f**) Br:Si = 2:2, (**g**) I:Si = 2:2, and (**h**) At:Si = 2:2. Green and blue circles represent the contribution of passivated Si atoms and halogen adatoms, respectively.

valence states between the Fermi level and the top of valence bands belong to free holes. Also, the energy bands near the Fermi level with a weaker dispersion are mainly contributed by the non-passivated Si-$3p_z$ orbitals [Fig. 3(c,d)], revealing that the low-lying energy bands gradually changed from the σ bands to the π bands. Besides, the middle-energy σ band of Si-($3p_x$ and $3p_y$) orbitals in pristine silicene [Fig. 3(a)] is located ~ −0.3 eV [Fig. 3(c)] and ~ −0.7 eV [Fig. 3(d)], reflecting a small variation in Si-Si bondings under these low-concentration adsorptions. Furthermore, such middle-energy σ bands are contributed by both passivated Si atoms and

non-passivated Si atoms, in which the latter atoms mainly contribute to the bands in the 11% system because of its higher concentration. Notably, the direct energy gap in the 100% system becomes indirect when the concentration reduces up to 25% [Table 1], and any halogen concentration lower than the critical concentration of 11% becomes the p-type metals. This remains true for most of the halogen adatoms. These revealed band features are sufficient to comprehend the concentration-dependent electronic properties.

In the single-side adsorptions, the destruction of the mirror symmetry [Fig. 1(b)] creates the valence energy bands intersecting with the Fermi level, in which the Fermi level is situated at the valence band, so the unoccupied valence states between the Fermi level and the half-occupied valence bands belong to free holes [Fig. 4]. As a result, these systems can also be regarded as the p-type metals. The full single-side adsorption cases [Fig. 4(a,d,f–h)] possess valence parabolic bands intersecting with the Fermi level, which are only related to the three non-passivated Si atoms [gray circles in Fig. 1(b)] nearest to the passivated Si atoms [red circles in Fig. 1(b)]. The parabolic dispersion change to the partially flat bands when the concentration declines, as shown in Fig. 4(b/e,c) for 12.5% and 5.6% systems, respectively. Furthermore, the π bondings between non-passivated Si atoms and passivated Si atoms [Fig. 1(b)] is seriously suppressed owing to the high charge transfer from the latter Si atoms and the halogen adatoms. This affirms that the non-passivated Si atoms can not form the extended π electronic states via the interaction with the passivated Si atoms. The clear discrepancy between the single-side and double-side adsorption cases is the valence energy bands intersecting with the Fermi level. Also, the halogen-induced weakly dispersed bands in the double-side adsorption cases [Fig. 3] reduce in number due to its decreased concentration [Fig. 4].

As compared with the pristine case [Fig. 3(a)], the Dirac cone structure is seriously distorted in the fully fluorinated case [Fig. 3(b)], and thoroughly destroyed in other cases, mainly owing to the seriously destruction or termination of the π bondings. Also, there exist other similar features, such as the recovery of low-energy π bands in the low-concentration systems, the adatom-modified middle-energy σ bands, and the halogen-induced weakly dispersed bands at deep energies. When the concentration decreases, both 5.6% single-side [Fig. 4(c)] and 11% double-side [Fig. 3(d)] systems show the low-lying π bands with large energy widths. These low-energy π bands are mainly contributed by the non-passivated Si-3p$_z$ orbitals, indicating that the π bondings are recovered among the Si atoms. The middle-energy σ bands (-0.2 eV$--3.5$ eV) [Figs 3(b–d) and 4(a–c)] are very similar to each other in terms of their band width, initiated energy, and orbital contribution, mainly owing to the hardly affected σ bondings. In addition, the halogen-related weakly dispersed bands are confined at similar energies in both single-side and double-side systems since the stable halogen-Si bondings are insensitive with the halogen concentrations (discussed in geometric structure section). That is to conclude that the broken geometric symmetries hardly have an impact on the aforementioned similar features.

To date, ARPES is an unique tool to verify the band structures. This experimental equipment can directly measure the direction, speed, and scattering process of valence electrons in the sample being studied. The high-resolution ARPES experiments have successfully verified the feature-rich band structures of graphenes on Ir(111)[58], few-layer graphenes[59], halogenated graphenes[60], 1D graphene nanoribbons[61], monolayer silicenes[35], hydrogenated silicenes[62], and multilayer silicene nanoribbons[63]. Apparently, similar ARPES measurements can be utilized to examine the feature-rich band structures after halogen adsorptions, including the destruction or recovery of low-energy π bands, the halogen-induced weakly dispersed bands at deep energies, and the valence energy bands intersecting with the Fermi level.

Spatial spin distribution. The highly geometric symmetry in the double-side adsorption cases [Fig. 1(a)] thoroughly destroys the spatial spin orientation, so that their energy bands are degenerate. When the geometric symmetry no longer exists [Fig. 1(b)], the spatial spin density distributions can be performed in the single-side adsorption cases, leading to the spin-splitting energy bands. Only except for the 50% fluorinated system [Fig. 4(a)] exhibits the degenerate parabolic band. The other 50% systems have the spin-splitting parabolic bands, which can clearly observe near the Fermi level, as shown by red (spin up) and black (spin down) curves in Fig. 4(d,f–h). These spin-splitting parabolic bands are mainly contributed by the non-passivated Si atoms, verified by the spatial spin density distributions near the non-passivated Si atoms (pure spin up configuration) [Fig. 5(a–c)]. However, the spin-splitting bands become weaker in the 12.5% systems [Fig. 4(b,e)]. This indicates that the spin-up and spin-down states can co-exist in its spin density distributions under the decrease of the halogen concentration (spin up and spin down mixed configuration), as shown by red (spin up state) and blue (spin down state) balls in Fig. 5(d–f). The difference in the spin up and spin down states directly determines the strength of the net magnetic moments, i.e., $0.72\,\mu_B$, $0.89\,\mu_B$, and $0.79\,\mu_B$ in the 50% systems and $0.64\,\mu_B$, $0.67\,\mu_B$, and $0.45\,\mu_B$ in the 12.5% systems [Table 2]. Notably, the spin density distributions are fully absence at the critical concentration of 5.6% (vanishing the net magnetic moment in Table 2), thus its energy bands are highly degenerate [Fig. 4(c)]. Furthermore, any halogen concentration beyond the critical concentration results in the absence of the spin density distributions. This remains true for all halogen adatoms. The single-side adsorption-induced magnetic properties on the silicene surface can be verified by the spin-polarized STM.

Spatial charge distribution. The spatial charge density distribution (ρ) can illustrate the strength of the Si-Si and halogen-Si bondings, as shown in Fig. 6(a–g). ρ displays a strong σ bonding between two Si atoms in the pristine silicene [Fig. 6(a)] or two non-passivated Si atoms in the low-concentration systems [Fig. 6(f,g)], as presented by the enclosed black rectangle. The strength of such σ bonding becomes weaker when Si atoms are bonded to halogen adatoms, as indicated by enclosed gray rectangle in Fig. 6(b–g), resulting in the extended Si-Si bond length. This accounts for the similarity in the adatom-modified middle-energy σ bands between the single-side and double-side adsorption cases. Away from the horizontal line between two Si atoms, ρ is lowered; however, its charge distribution is extended, evidencing for the π-electronic states, as shown by enclosed red rectangle in Fig. 6(a,f,g). Nevertheless, hardly extended states, corresponding to the π-charge-depleted region, are
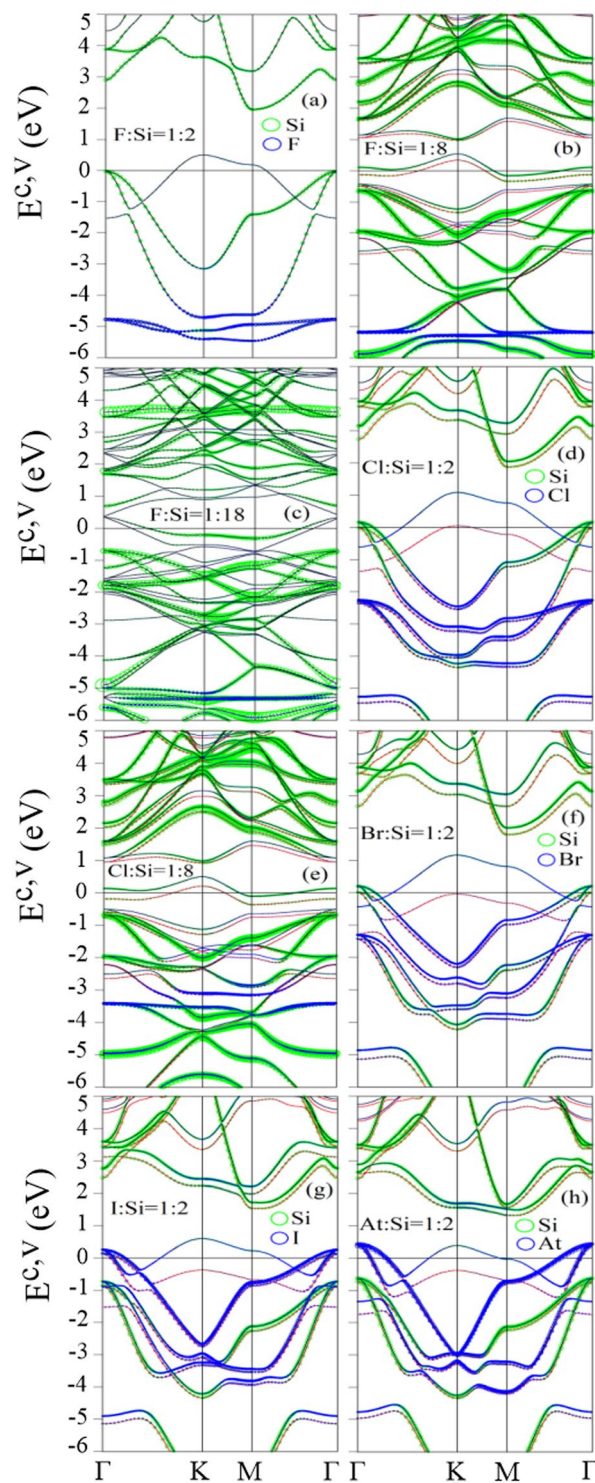
Figure 4. Similar plot as Fig. 3, but shown for single-side adsorptions of (**a**) F:Si = 1:2, (**b**) F:Si = 1:8, (**c**) F:Si = 1:18, (**d**) Cl:Si = 1:2, (**e**) Cl:Si = 1:8, (**f**) Br:Si = 1:2, (**g**) I:Si = 1:2, and (**h**) At:Si = 1:2. Red and black curves, respectively, correspond to the spin-up and spin-down energy bands.

perceived between the passivated and non-passivated Si atoms (enclosed purple rectangle in Fig. 6(d–g)). This charge distribution is similar to isolated Si atoms and evidences for the destruction of π bondings. Furthermore, the charge density of halogen-Si bondings is much higher than that of Si-Si bondings, as indicated by the dashed black rectangle in Fig. 6(b–g). Thus, such stable halogen-Si bondings are insensitive to the halogen concentrations. This illustrates that the halogen-Si bonding-induced weakly dispersed bands are limited to similar energies in both single-side and double-side systems. In order to further understand the detailed charge transfers among all orbitals, the charge density difference ($\triangle\rho$) is presented in Fig. 6(h–m). $\triangle\rho$ is created by subtracting
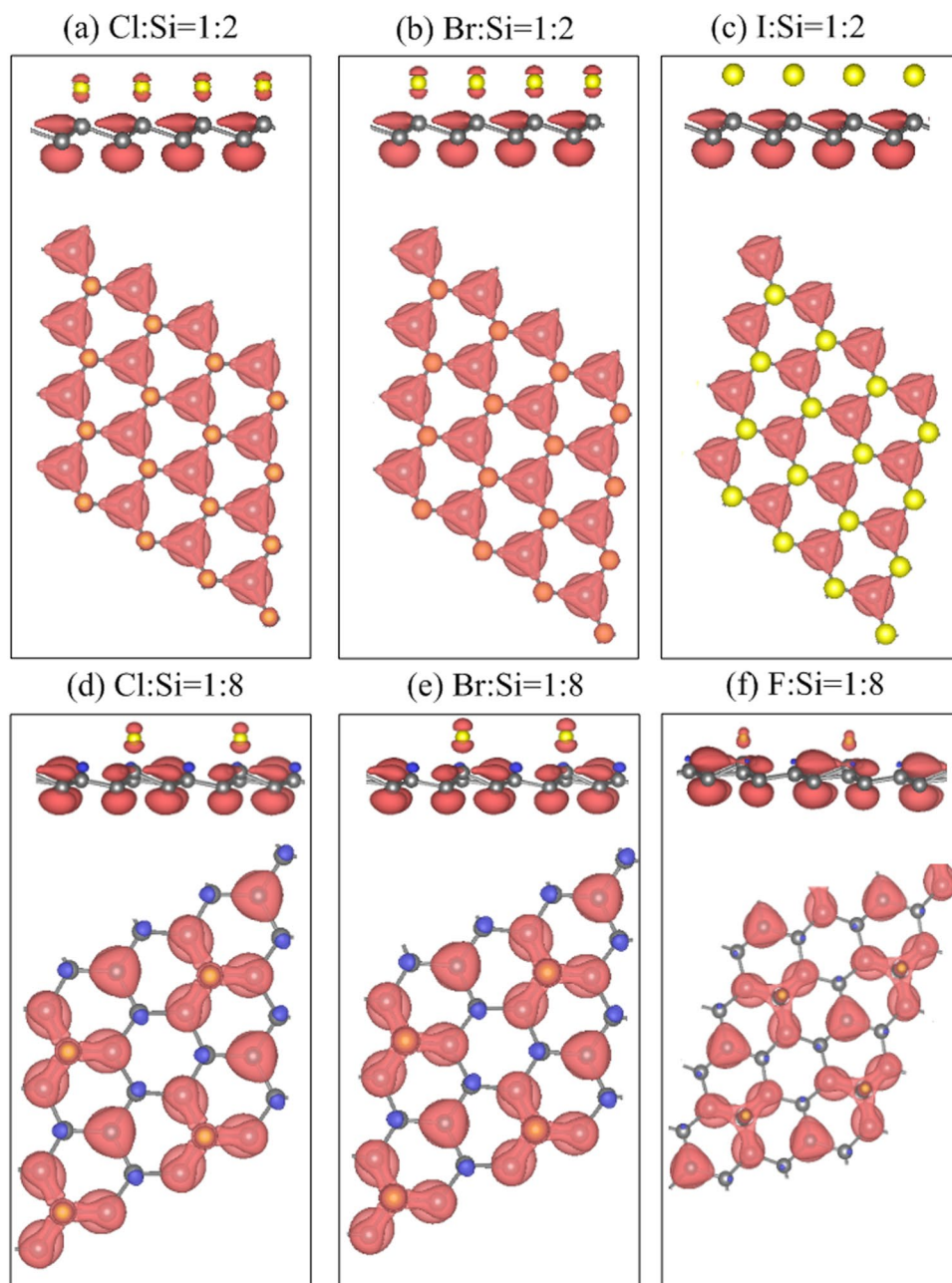
Figure 5. Spatial spin density distribution with side-view and top-view for (**a**) Cl:Si = 1:2, (**b**) Br:Si = 1:2, (**c**) I:Si = 1:2, (**d**) Cl:Si = 1:8, (**e**) Br:Si = 1:8, and (**f**) F:Si = 1:8. Red and blue isosurfaces, respectively, correspond to the spin-up and spin-down orientations.

the charge density of the pristine silicene and isolated halogen adatoms from that of the composite system. All the halogen-adsorbed systems exhibit a high charge transfer from Si atoms to halogen adatoms to form the stable halogen-Si bondings (dashed black rectangle in Fig. 6(h–m)). Also, such clear variation of charge density accounts for a weaker bond strength of the nearest Si-Si bonds around the halogen adatoms.

Diverse density of states.   The orbital-projected density of states (DOSs) is used to verify the band structures and comprehend the orbital hybridizations in the chemical bonds. For pristine silicene [Fig. 7(a)], the low-energy DOSs exhibits the vanished value at $E_F = 0$, V-shaped structure, and two symmetric logarithmic divergent peaks at $E^{c,v} \sim \pm 1$ eV, are induced by Si-$3p_z$ orbitals (purple solid curve in Fig. 7(a)). They respectively originate from the negligible-energy gap, the Dirac cone structure, and the saddle points of π bands at the M point [Fig. 3(a)]. The middle-energy DOSs shows a shoulder structure at -1 eV and a prominent peak at -2.6 eV, resulting from the maximum point and the saddle point of σ bands, respectively. They are mainly contributed by Si-($3p_x$ and $3p_y$) orbitals (green and blue solid curves in Fig. 7(a)). Moreover, the hybridization between Si-3s (red solid curve in Fig. 7(a)) and Si-$3p_z$ orbitals creates a prominent peak at -3.2 eV, coming from the partially flat
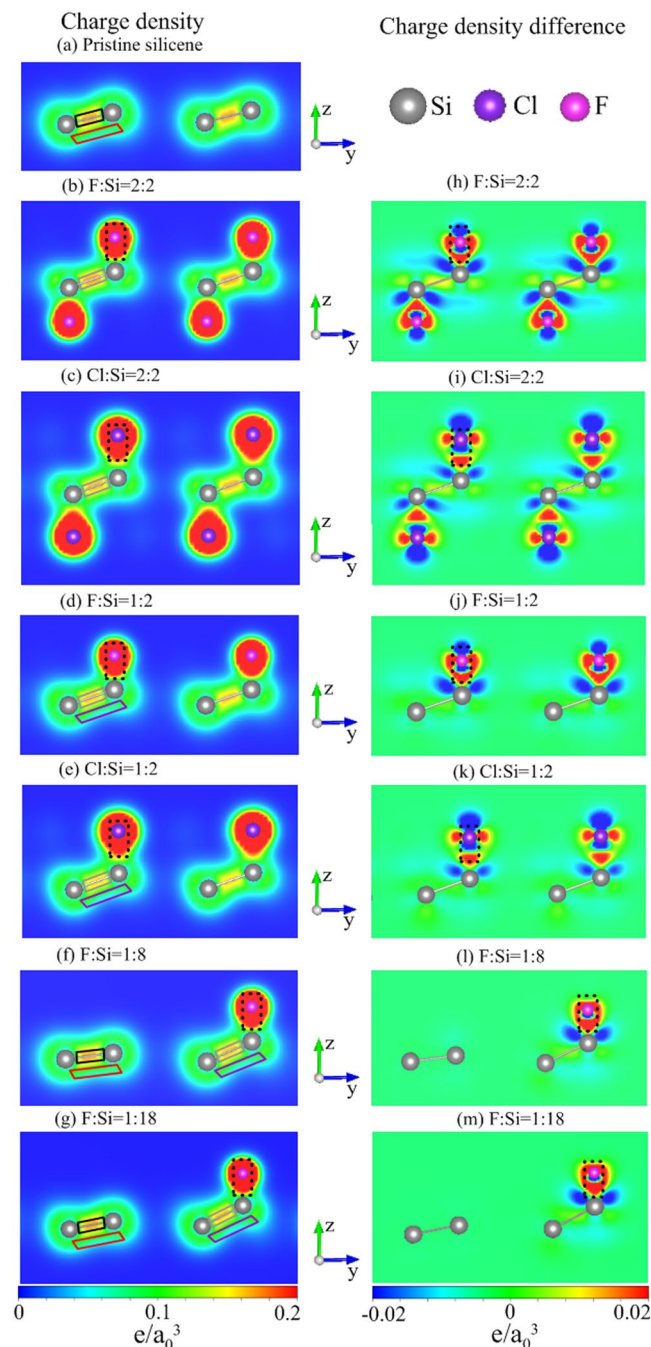
Figure 6. Spatial charge density at the left-hand side for (**a**) pristine silicene and halogenated silicene of (**b**) F:Si = 2:2, (**c**) Cl:Si = 2:2, (**d**) F:Si = 1:2, (**e**) Cl:Si = 1:2, (**f**) F:Si = 1:8, and (**g**) F:Si = 1:18; charge density difference at the right-hand side for (**h**) F:Si = 2:2, (**i**) Cl:Si = 2:2, (**j**) F:Si = 1:2, (**k**) Cl:Si = 1:2, (**l**) F:Si = 1:8, and (**m**) F:Si = 1:18. a_0 is Bohr radius.

band with an initiated energy at the Γ point. These features further indicate that the interactions between π and σ bands at low energy are weak.

The low-energy DOSs is strongly modified after halogen adsorptions. Under the full double-side adsorption cases, it shows the vacant states at specific region centered at $E_F = 0$ in the fluorinated [Fig. 7(b)], chlorinated [Fig. 7(e)], brominated [Fig. 7(f)], and iodinated systems [Fig. 7(g)], coming from the finite gap feature in its corresponding band structures. Otherwise, the finite value of DOSs at $E_F = 0$ comes to exist in the astatinated system [Fig. 7(h)] as result of the semi-metallic behavior [Fig. 3(h)]. The middle-energy DOSs displays a shoulder structure at $-0.2\,\mathrm{eV}$ and the prominent peak at $-1.5\,\mathrm{eV}$, are dominated by Si-($3p_x$ and $3p_y$) orbitals (green and blue solid curves in Fig. 7(b)), are very similar to that of pristine silicene [Fig. 7(a)], accounting for the adatom-modified middle-energy σ band. Such modified middle-energy DOSs structure is also observed in Fig. 7(e–h). Furthermore, the extra strong peaks at deep energies are dominated by halogen-($2p_x$ and $2p_y$) orbitals
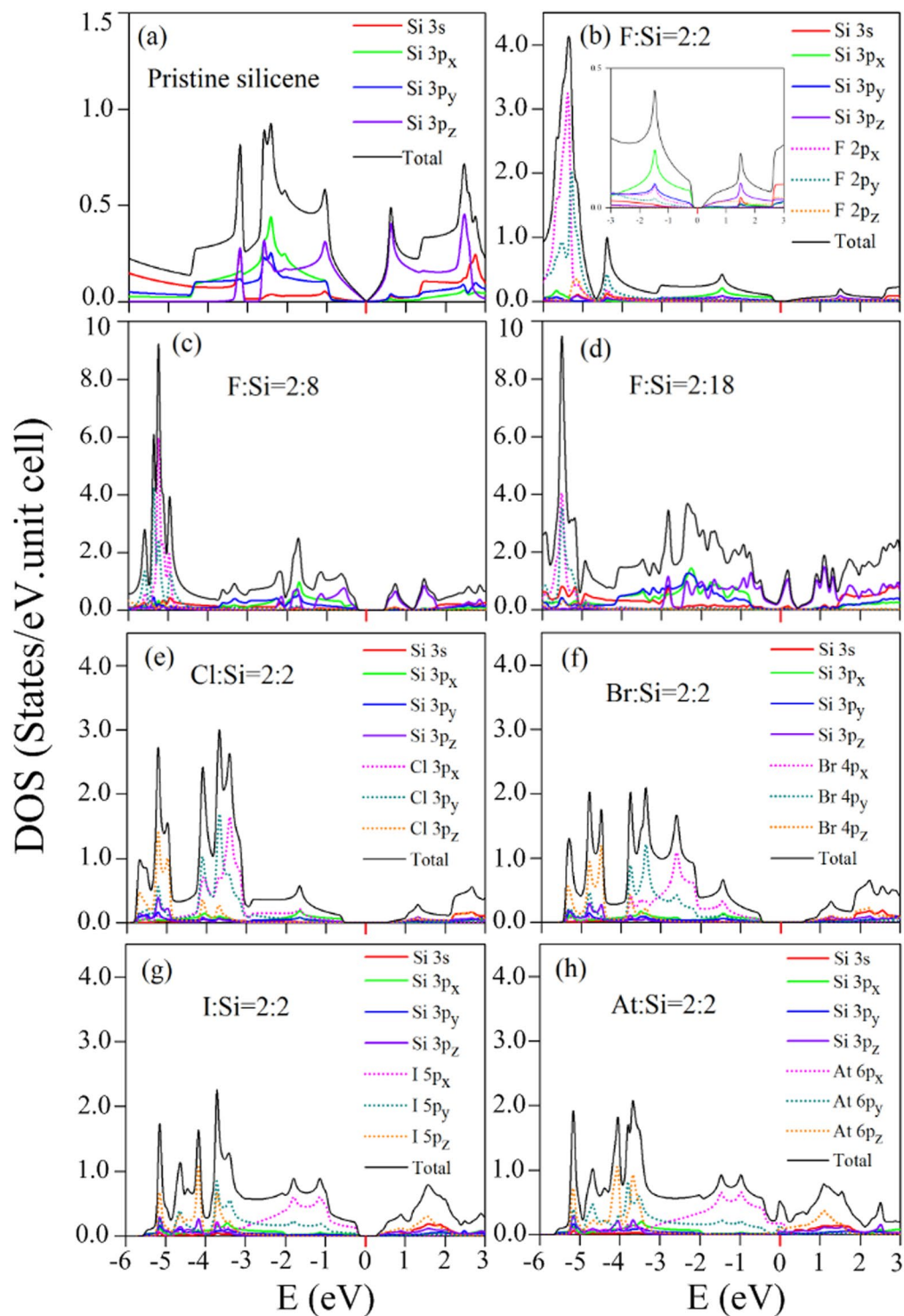
Figure 7. Orbital-projected DOSs for (**a**) pristine silicene; double-side adsorptions of (**b**) F:Si = 2:2, (**c**) F:Si = 2:8, (**d**) F:Si = 2:18, (**e**) Cl:Si = 2:2, (**f**) Br:Si = 2:2; (**g**) I:Si = 2:2, and (**h**) At:Si = 2:2.

[Fig. 7(b)], standing for the halogen-related weakly dispersed bands at deep energies [Fig. 3(b)]. These strong peaks become weaker and dominate at higher energies as their atomic numbers increasing [Fig. 7(e–h)]. When the halogen concentration declines, three low-energy prominent peaks appear at −0.6 eV, 0.8 eV, and 1.4 eV in the 25% system [Fig. 7(c)]. The bandwidth of these prominent peaks about 0.6 eV, and their states are related to Si-$3p_z$ orbitals (purple solid curve). Also, their middle-energy DOSs are contributed by Si-($3p_x$ and $3p_y$) orbitals; however, the single peak structure in the full adsorption case [Fig. 7(b)] separate into several sub-peaks owing to an enhancement of sub-bands. At the critical concentration of 11%, most of the low-energy DOSs within ±1 eV are mainly dominated by the non-passivated Si-$3p_z$ orbitals [Fig. 7(d)], illustrating a π bandwidth similar to the
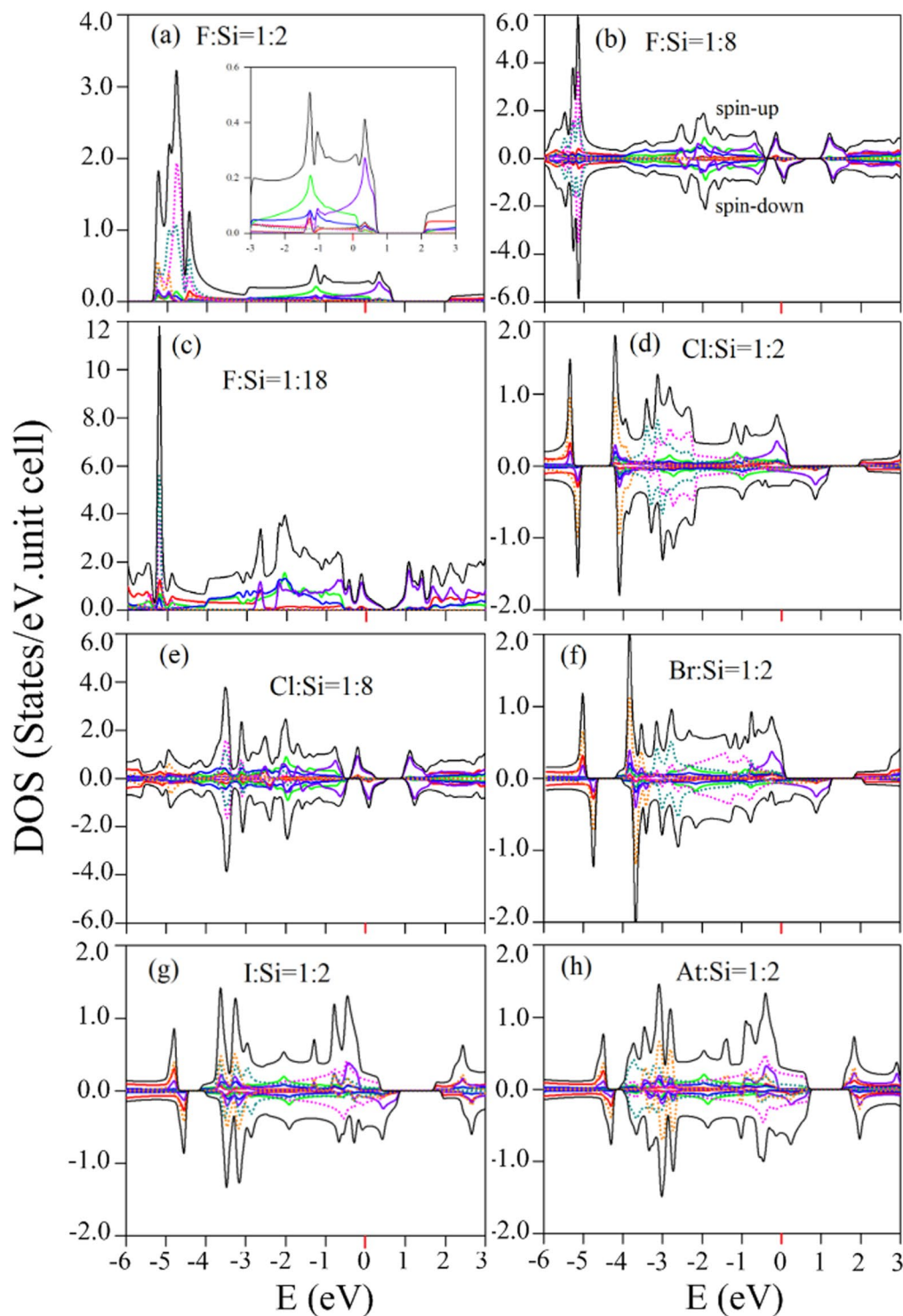
Figure 8. Similar plot as Fig. 7, but shown for single-side adsorptions of (**a**) F:Si = 1:2, (**b**) F:Si = 1:8, (**c**) F:Si = 1:18, (**d**) Cl:Si = 1:2, (**e**) Cl:Si = 1:8; (**f**) Br:Si = 1:2, (**g**) I:Si = 1:2, and (**h**) At:Si = 1:2.

pristine case [Fig. 7(a)]. This evidences the recovery of low-energy π bands in low-concentration systems. Also, these two low-concentration systems show the halogen-dominated extra strong peaks at deep energies similar to the 100% system [Fig. 7(b)]. However, the intensity of these deep-energy extra strong peaks is roughly proportional to the halogen concentration.

The fundamental features of DOSs in the single-side and double-side adsorption cases are the strong peaks, which are closely associated with the Si- and halogen-related bondings. The similarities are identified between the single-side cases and its corresponding double-side adsorptions, including the extended low-energy π band widths [Figs 7(d) and 8(c)], the three Si-3p$_z$ orbital-related prominent peaks within -1 eV to 2 eV [Figs 7(c) and 8(b)],

the Si-(3p$_x$ and 3p$_y$) orbital-dominated single-peak structure [Figs 7(b) and 8(a)], and the halogen-related extra strong peaks at deep energies Figs 7(b) and 8(a); 7(c) and 8(b); 7(d) and 8(c)]. These extra strong peaks are confined at the same energy range; however, their intensities are gradually declined as the halogen concentration reduced. The similar DOSs features is also found in other halogen-adsorption cases [Figs 7(e–h) and 8(d–h)]. On the other hand, the breaking of the mirror symmetry in the single-side adsorption cases leads to a critical discrepancy, i.e., there exist the finite value of DOSs at the Fermi level as a result of the metallic behaviors [Fig. 8(a–h)]. Also, the asymmetric prominent peaks near the Fermi level [Fig. 8(b,d–h)] provide a very useful information in confirming the spin-splitting energy bands [Fig. 3].

On the experimental side, the STS measurements, where the tunneling differential conductance (dI/dV) is proportional to DOSs, can provide sufficient information in examining the special features in DOSs. High-resolution STS measurements are able to distinguish the semiconducting, semi-metallic and metallic behavior. Moreover, they can be used to identify the close relations between the electronic energy spectra and the orbital hybridizations of the chemical bonds. To date, such experimental measurements have been successfully used to confirm the electronic band structure near the Fermi level and the dimension-diversified van Hove singularities in monolayer graphene[64] and few-layer graphene systems[65–67], 1D graphene nanoribbons[68,69], adatom-adsorbed graphene[70], monolayer silicene[71], and hydrogenated silicene[72]. Obviously, the theoretical predictions on the halogen-diversified DOSs can be thoroughly affirmed by the STS experiments, including the vanishing or existing of the finite value of DOSs at the Fermi level, the Si- or halogen-dominated strong peaks, and the halogen-modified σ shoulder structures. Furthermore, spin-polarized STS is available for verifying the asymmetric peaks near the Fermi level in DOSs.

Conclusion

The geometric, magnetic, and electronic properties of halogen-adsorbed silicene are studied by the ab initio calculations. The rich physical and chemical properties are diversified by the halogen concentrations. Specifically, the stable halogen-Si bondings are the critical factor in affecting the geometric structures, spatial spin density distributions, spatial charge density distributions and its variations, atom-dominated energy bands, and DOSs. The transfer of electrons from Si atoms to halogen adatoms leads to variations in the charge density distributions in the chemical bonds, directly resulting in the drastically modulation of the magnetic and electronic properties. The rich band structures after halogen adsorptions are highlighted by the destruction or recovery of low-lying π bands, the halogen-induced weakly dispersed bands at deep energies, and the valence energy bands with/without spin-splitting intersecting with the Fermi level. The first feature is determined by the competition between the halogen-Si bondings and the weak sp^3 hybridization. The energy gap determined by the σ bands is indirect in the full double-side systems. As the concentration declines, the low-lying π bands gradually recover, rendering the gap size smaller with an indirect behavior in the 25% system, and even though becoming the p-type metals at the critical concentration of 11%. The second feature, mainly owing to the stable halogen-Si bonding insensitive with the halogen concentrations, is the similar characteristic of both single-side and double-side adsorptions. The third feature, originating from the broken mirror symmetry, is a distinct characteristic in the single-side adsorptions. Also, the spatial spin density distributions only reveal in the specific single-side systems, resulting in the spin-splitting energy bands or the asymmetric prominent peaks near the Fermi level in DOSs. The above-mentioned band properties are fully confirmed by their DOSs, including the vacant region centered at the Fermi level, the recovery of π band-related low-energy prominent peaks, the halogen-related extra strong peaks at deep energies, and the finite value of DOSs at the Fermi level. The feature-rich band structures and the diverse DOSs can be verified by the ARPES and STS measurements, respectively. The concentration-tuned diverse magnetic and electronic properties of halogen-adsorbed silicene are very potential for applications in both nanoelectronics and spintronics.

Method

The diverse magnetic and electronic properties of halogen-adsorbed silicene are investigated by the spin-polarized density functional theory (DFT) implemented in VASP (Vienna ab initio simulation package)[73]. The exchange and correlation energies, which come from the many-particle electron-electron interactions, are evaluated by the Perdew-Burke-Ernzerhof (PBE) functional under the generalized gradient approximation[74]. Furthermore, the projector-augmented wave (PAW) pseudopotentials can characterize the electron-ion interactions. The plane-waves basis set with a kinetic energy cutoff of 500 eV is utilized to calculate wave functions and state energies. A vacuum space of 10 Å is inserted between periodic planes to avoid the interaction of two planes. The first Brillouin zone is sampled by $12 \times 12 \times 1$ and $100 \times 100 \times 1$ k-point meshes within the Monkhorst-Pack scheme for geometric optimizations and electronic structure calculations, respectively. Such points are sufficient for obtaining reliable DOSs. The convergence for energy is set to be 10^{-5} eV between two consecutive steps, and the maximum Hellmann-Feynman force acting on each atom is less than 0.01 eV/Å during the ionic relaxations.

References

1. Novoselov, K. et al. Electric field effect in atomically thin carbon films. Science 306, 666–669 (2004).
2. Geim, A. K. & Novoselov, K. S. The rise of graphene. Nature Mater 6, 183–191 (2007).
3. Katsnelson, M. I., Novoselov, K. S. & Geim, A. K. Chiral tunnelling and the Klein paradox in graphene. Nature physics 9, 620–625 (2006).
4. Berger, C. et al. Electronic confinement and coherence in patterned epitaxial graphene. Science 312, 1191–1196 (2006).
5. Zhang, Y., Tan, Y. W., Stormer, H. L. & Kim, P. Experimental observation of the quantum Hall effect and Berry's phase in graphene. Nature 438, 201–204 (2005).
6. Tran, N. T. T., Nguyen, D. K., Lin, S. Y., Gumbs, G. & Lin, M. F. Fundamental properties of transition-metals-adsorbed graphene. ChemPhysChem, 201900614 (2019).

7. Nguyen, D. K. *et al*. Fluorination-enriched electronic and magnetic properties in graphene nanoribbons. *Physical Chemistry Chemical Physics* **19**, 20667–20676 (2017).
8. Nguyen, D. K., Tran, N. T. T., Nguyen, T. T. & Lin, M. F. Diverse Electronic and Magnetic Properties of Chlorination-Related Graphene Nanoribbons. *Scientific reports* **8**, 17859 (2018).
9. Eda, G., Fanchini, G. & Chhowalla, M. Large-area ultrathin films of reduced graphene oxide as a transparent and flexible electronic material. *Nature nanotechnology* **3**, 270–274 (2008).
10. Robinson, J. T., Perkins, F. K., Snow, E. S., Wei, Z. & Sheehan, P. E. Reduced graphene oxide molecular sensors. *Nano letters* **9**, 3137–3140 (2008).
11. Elias, D. C. *et al*. Control of graphene's properties by reversible hydrogenation: evidence for graphane. *Science* **323**, 610–613 (2009).
12. Sahin, H., Ataca, C. & Ciraci, S. Magnetization of graphane by dehydrogenation. *Applied Physics Letters* **95**, 222510 (2009).
13. Topsakal, M., Cahangirov, S. & Ciraci, S. The response of mechanical and electronic properties of graphane to the elastic strain. *Applied Physics Letters* **96**, 091912 (2010).
14. Robinson, J. T. *et al*. Properties of fluorinated graphene films. *Nano letters* **10**, 3001–3005 (2010).
15. Sahin, H., Topsakal, M. & Ciraci, S. Structures of fluorinated graphene and their signatures. *Physical Review B* **83**, 115432 (2011).
16. Li, B. *et al*. Photochemical chlorination of graphene. *ACS nano* **5**, 5957–5961 (2011).
17. Sahin, H. & Ciraci, S. Chlorine adsorption on graphene: Chlorographene. *The Journal of Physical Chemistry C* **116**, 24075–24083 (2012).
18. Jin, C., Lin, F., Suenaga, K. & Iijima, S. Fabrication of a freestanding boron nitride single layer and its defect assignments. *Physical review letters* **102**, 195505 (2009).
19. Ci, L. *et al*. Atomic layers of hybridized boron nitride and graphene domains. *Nature materials* **9**, 430 (2010).
20. Topsakal, M., Aktürk, E. & Ciraci, S. First-principles study of two-and one-dimensional honeycomb structures of boron nitride. *Physical Review B* **79**, 115442 (2009).
21. Novoselov, K. S. Graphene: materials in the flatland (Nobel Lecture). *Angewandte Chemie International Edition* **50**, 6986–7002 (2011).
22. Dávila, M. E. & Le Lay, G. Few layer epitaxial germanene: a novel two-dimensional Dirac material. *Scientific reports* **6**, 20714 (2016).
23. Nijamudheen, A., Bhattacharjee, R., Choudhury, S. & Datta, A. Electronic and chemical properties of germanene: the crucial role of buckling. *The Journal of Physical Chemistry C* **119**, 3802–3809 (2015).
24. Zhu, F. F. *et al*. Epitaxial growth of two-dimensional stanene. *Nature materials* **14**, 1020 (2015).
25. Saxena, S., Chaudhary, R. P. & Shukla, S. Stanene: atomically thick free-standing layer of 2D hexagonal tin. *Scientific reports* **6**, 31073 (2016).
26. Rivero, P., Yan, J. A., García-Suárez, V. M., Ferrer, J. & Barraza-Lopez, S. Stability and properties of high-buckled two-dimensional tin and lead. *Physical Review B* **90**, 241408 (2014).
27. Perepichka, D. F. & Rosei, F. Silicon nanotubes. *Small* **2**, 22–25 (2006).
28. Marsen, B. & Sattler, K. Fullerene-structured nanowires of silicon. *Physical Review B* **60**, 11593 (1999).
29. Vogt, P. *et al*. Silicene: compelling experimental evidence for graphene-like two-dimensional silicon. *Physical review letters* **108**, 155501 (2012).
30. Feng, B. *et al*. Evidence of silicene in honeycomb structures of silicon on Ag (111). *Nano letters* **12**, 3507–3511 (2012).
31. Gao, J. & Zhao, J. Initial geometries, interaction mechanism and high stability of silicene on Ag (111) surface. *Scientific reports* **2**, 861 (2012).
32. Meng, L. *et al*. Buckled silicene formation on Ir (111). *Nano letters* **13**, 685–690 (2013).
33. Takeda, K. & Shiraishi, K. Theoretical possibility of stage corrugation in Si and Ge analogs of graphite. *Physical Review B* **50**, 14916 (1994).
34. Cahangirov, S., Topsakal, M., Aktürk, E., Sahin, H. & Ciraci, S. Two-and one-dimensional honeycomb structures of silicon and germanium. *Physical review letters* **102**, 236804 (2009).
35. Lee, C. C., Fleurence, A., Yamada-Takamura, Y., Ozaki, T. & Friedlein, R. Band structure of silicene on zirconium diboride (0001) thin-film surface: Convergence of experiment and calculations in the one-Si-atom Brillouin zone. *Physical Review B* **90**, 075422 (2014).
36. Chen, L. *et al*. Evidence for Dirac fermions in a honeycomb lattice based on silicon. *Physical review letters* **109**, 056804 (2012).
37. Tao, L. *et al*. Silicene field-effect transistors operating at room temperature. *Nature nanotechnology* **10**, 227 (2015).
38. Liu, C. C., Jiang, H. & Yao, Y. Low-energy effective Hamiltonian involving spin-orbit coupling in silicene and twodimensional germanium and tin. *Physical Review B* **84**, 195430 (2011).
39. Liu, C. C., Feng, W. & Yao, Y. Quantum spin Hall effect in silicene and two-dimensional germanium. *Physical review letters* **107**, 076802 (2011).
40. Ezawa, M. A topological insulator and helical zero mode in silicene under an inhomogeneous electric field. *New Journal of Physics* **14**, 033003 (2012).
41. Drummond, N. D., Zolyomi, V. & Falkó, V. I. Electrically tunable band gap in silicene. *Physical Review B* **85**, 075423 (2012).
42. Ezawa, M. Valley-polarized metals and quantum anomalous Hall effect in silicene. *Physical review letters* **109**, 055502 (2012).
43. Lin, S. Y., Chang, S. L., Tran, N. T. T., Yang, P. H. & Lin, M. F. H-Si bonding-induced unusual electronic properties of silicene: a method to identify hydrogen concentration. *Physical Chemistry Chemical Physics* **17**, 26443–26450 (2015).
44. Sahin, H. & Peeters, F. M. Adsorption of alkali, alkaline-earth, and 3d transition metal atoms on silicene. *Physical Review B* **87**, 085423 (2013).
45. Sivek, J., Sahin, H., Partoens, B. & Peeters, F. M. Adsorption and absorption of boron, nitrogen, aluminum, and phosphorus on silicene: Stability and electronic and phonon properties. *Physical Review B* **87**, 085444 (2013).
46. Gao, N., Zheng, W. T. & Jiang, Q. Density functional theory calculations for two-dimensional silicene with halogen functionalization. *Physical Chemistry Chemical Physics* **14**, 257–261 (2012).
47. Zhang, W. B., Song, Z. B. & Dou, L. M. The tunable electronic structure and mechanical properties of halogenated silicene: a first-principles study. *Journal of Materials Chemistry C* **3**, 3087–3094 (2015).
48. Li, W. *et al*. Ordered chlorinated monolayer silicene structures. *Physical Review B* **93**, 155410 (2016).
49. Tran, N. T. T., Nguyen, D. K., Glukhova, O. E. & Lin, M. F. Coverage-dependent essential properties of halogenated graphene: A DFT study. *Scientific reports* **7**, 17858 (2017).
50. Xue, J. *et al*. Scanning tunnelling microscopy and spectroscopy of ultra-flat graphene on hexagonal boron nitride. *Nature materials* **10**, 282 (2011).
51. Biedermann, L. B., Bolen, M. L., Capano, M. A., Zemlyanov, D. & Reifenberger, R. G. Insights into few-layer epitaxial graphene growth on 4H-SiC(0001) substrates from STM studies. *Physical Review B* **79**, 125411 (2009).
52. Balog, R. *et al*. Atomic hydrogen adsorbate structures on graphene. *Journal of the American Chemical Society* **131**, 8744–8745 (2009).
53. Johns, J. E. & Hersam, M. C. Atomic covalent functionalization of graphene. *Accounts of chemical research* **46**, 77–86 (2012).
54. Tao, C. *et al*. Spatially resolving edge states of chiral graphene nanoribbons. *Nature Physics* **7**, 616 (2011).
55. Aufray, B. *et al*. Graphene-like silicon nanoribbons on Ag (110): A possible formation of silicene. *Applied Physics Letters* **96**, 183102 (2010).
56. Medina, D. B., Salomon, E., Le Lay, G. & Angot, T. Hydrogenation of silicene films grown on Ag (111). *Journal of Electron Spectroscopy and Related Phenomena* **219**, 57–62 (2017).

57. Chen, H. D., Chien, K. H., Lin, C. Y., Chiang, T. C. & Lin, D. S. Few-layer silicon films on the Ag (111) surface. *The Journal of Physical Chemistry C* **120**, 2698–2702 (2016).
58. Pletikosić, I. *et al.* Dirac cones and minigaps for graphene on Ir (111). *Physical Review Letters* **102**, 056808 (2009).
59. Sutter, P., Hybertsen, M. S., Sadowski, J. T. & Sutter, E. Electronic structure of few-layer epitaxial graphene on Ru (0001). *Nano letters* **9**, 2654–2660 (2009).
60. Walter, A. L. *et al.* Highly p-doped epitaxial graphene obtained by fluorine intercalation. *Applied Physics Letters* **98**, 184102 (2011).
61. Ruffieux, P. *et al.* Electronic structure of atomically precise graphene nanoribbons. *ACS Nano* **6**, 6930–6935 (2012).
62. Wang, W., Olovsson, W. & Uhrberg, R. I. G. Band structure of hydrogenated silicene on Ag (111): Evidence for half-silicane. *Physical Review B* **93**, 081406 (2016).
63. De Padova, P. *et al.* Multilayer silicene nanoribbons. *Nano letters* **12**, 5500–5503 (2012).
64. Gao, L. Probing Electronic Properties of Graphene on the Atomic Scale by Scanning Tunneling Microscopy and Spectroscopy. *Graphene and 2D Materials* **1**, 1 (2014).
65. Lauffer, P. *et al.* Atomic and electronic structure of few-layer graphene on SiC(0001) studied with scanning tunnelling microscopy and spectroscopy. *Physical Review B* **77**, 155426 (2008).
66. Yankowitz, M., Wang, F., Lau, C. N. & LeRoy, B. J. Local spectroscopy of the electrically tunable band gap in trilayer graphene. *Physical Review B* **87**, 165102 (2013).
67. Pierucci, D. *et al.* Evidence for flat bands near the Fermi level in epitaxial rhombohedral multilayer graphene. *ACS nano* **9**, 5432–5439 (2015).
68. Huang, H. *et al.* Spatially resolved electronic structures of atomically precise armchair graphene nanoribbons. *Scientific reports* **2**, 983 (2012).
69. Söde, H. *et al.* Electronic band dispersion of graphene nanoribbons via Fourier-transformed scanning tunneling spectroscopy. *Physical Review B* **91**, 045429 (2015).
70. Gyamfi, M., Eelbo, T., Waśniowska, M. & Wiesendanger, R. Fe adatoms on graphene/Ru (0001): Adsorption site and local electronic properties. *Physical Review B* **84**, 113403 (2011).
71. Chiappe, D., Grazianetti, C., Tallarida, G., Fanciulli, M. & Molle, A. Local electronic properties of corrugated silicone phases. *Advanced Materials* **24**, 5088–5093 (2012).
72. Lin, C. *et al.* Direct observation of ordered configurations of hydrogen adatoms on graphene. *Nano letters* **15**, 903–908 (2015).
73. Kresse, G. & Furthmüller, J. Efficient iterative schemes for ab initio total-energy calculations using a plane-wave basis set. *Physical review B* **54**, 11169 (1996).
74. Perdew, J. P., Burke, K. & Ernzerhof, M. Generalized gradient approximation made simple. *Physical review letters* **77**, 3865 (1996).

Acknowledgements

Author Contributions

Duy Khanh Nguyen did numerical calculations and wrote the manuscript under the assistance of Ngoc Thanh Thuy Tran and the guidance of Ming-Fa Lin and Yu-Huang Chiu.

Additional Information

Competing Interests: The authors declare no competing interests.

Publisher's note Springer Nature remains neutral with regard to jurisdictional claims in published maps and institutional affiliations.